Improving the energy harvesting performance of clamped flexible plates using vortex shedding behind bluff bodies: a computational study

Xinyu Wang,[1] Xu Guo,[1] Yue Mei,[1, a)] and Chennakesava Kadapa[2, a)]

[1)]*Department of Engineering Mechanics, Dalian University of Technology, Dalian, China.*

[2)]*School of Computing Engineering and Built Environment, Edinburgh Napier University, Edinburgh EH10 5DT, Scotland, United Kingdom.*

(Dated: 29 August 2024)

This study assesses flow-induced vibrations of clamped flexible plates with the objective of improving their energy harvesting performance. Towards this, a rectangular bluff body is placed between the two clamped flexible plates to harness the vortices generated behind the bluff body. The strain energy of the plate is used as a measure of energy harvesting performance. Computational studies are performed for different parameters of interest, such as dimensions and material properties of the plate and dimensions and locations of the bluff body. The effects of these stated parameters on flow-induced vibration response and vortical structures are investigated, and the optimal values for the location and geometry of the bluff body, as well as the aspect ratio and Young's modulus of the plate for energy harvesting performance, are determined. The results show that vortex shedding from the bluff body strongly influences the dynamic behaviour and energy output of the flexible structures inside the wake region of the bluff body at different locations. Additionally, the aspect ratio and its effect on vorticity and energy harvesting are discussed in detail, along with the average displacement and average lift force experienced by the plates. The outcomes of this work offer significant insights into optimizing the design of clamped flexible plates for optimal energy generation by cleverly exploiting the vortex shedding behind fixed bluff bodies.

[a)]Authors to whom correspondence should be addressed: c.kadapa@napier.ac.uk or meiyue@dlut.edu.cn

I. INTRODUCTION

The limited availability of fossil fuel resources and their negative environmental impacts have motivated a significant research effort in the development of renewable energy. Owing to this, research on renewable energy from wind[1], solar[2], and ocean sources[3] has received increasing attention, and efforts to harvest energy from renewable resources have also risen substantially[4,5]. In recent years, scientists have focused on investigating ways to extract energy from different sources of vibration, particularly from coupled fluid-structure systems, which hold potential as a viable alternative. There are significant ongoing research efforts focussed on employing fluid-structure interactions (FSI) such as vortex-induced vibrations (VIV)[6,7], galloping[8] and flutter[9] to harvest energy, which forms the core of prototypes of flow energy harvesters. These fundamental mechanisms act as energy extraction mechanisms to produce electricity using displacement-based [10–12] or deformation-based conversion[13–16]. Among the various energy conversion mechanisms, those based on piezoelectric patches are the most widely used, where vibration energy is harnessed through the direct piezoelectric effect[17]. For example, Wang et al.[18] proposed a novel coupled VIV-galloping-based piezoelectric energy harvester with bluff bodies and studied the effect of two different bluff body shapes on the efficiency of the energy harvester.

A flag-flutter-based piezoelectric energy harvester is modeled based on fluid-structure interaction by Eugeni et al.[19], which demonstrates the possibility of harvesting energy from limit cycle oscillations by piezoelectric transduction. To enhance the energy harvesting performance of systems based on VIV or galloping instabilities, a variety of optimization strategies have been proposed, which suggested various performance enhancement measures, such as introducing a multistable nonlinear vibrational energy harvester [20,21], or utilizing designed models[22,23]. Hu et al.[24] experimentally investigated the energy harvesting performance of a circular cylinder with two small-size rod-shaped attachments and found that attaching two triangular rods to the main circular cylinder at circumferential locations 60° apart resulted in better energy harvesting performance. Zhao et al.[25] introduced a high-frequency mechanical stopper as a supplemental energy source and found that energy harvesting efficiency has been increased nearly twice.

The flow energy harvesting from fluid-flexible plate coupling systems using deflection-based energy conversion mechanisms have been investigated simultaneously [26–28]. Previous studies have focused on employing two basic configurations to investigate energy harvesting by flapping elastic plates. The first configuration [29,30] utilizes the flutter instability of the flexible plate to generate

self-sustained periodic vibration. However, high flow velocity is required to achieve good performance. Moreover, tuning the plate's dominant vibration mode shapes to coincide with its most energetic fluttering instability mode is highly challenging. The second configuration [31,32] consists of a flexible plate placed in the wake of a bluff body, which could show the flapping due to the interaction of shed vortices of the upstream bluff object. Compared with the first configuration, although the vortex generated by the bluff body induces large oscillations in the downstream flexible structure, placing a bluff body upstream increases the nonlinearity of the system and also reduces the amount of energy available from the fluid for harvesting. In particular, Singh et al.[33] investigated energy harvesting from flutter instabilities in flexible slender structures placed in axial flows and showed that power output can be optimized by tailoring the distribution of damping along the structure. Ryu et al.[30] analyzed the interaction of vortex shedding and inverted flags in terms of Reynolds number and bending stiffness. It was concluded that the maximum strain energy was obtained near the tail end; hence, it was recommended to attach piezoelectric patches near the trailing edge. Latif et al.[34], Mittal et al.[35], and Pineirua et al.[36] actuated the plate in its most energetic mode shape to maximize energy harvesting by controlling the flow conditions and the piezoelectric properties of the plate.

Most of the literature extensively studies flexible plates in cantilever configurations, that is, with a fixed leading end and free trailing end for energy harvesting under the influence of flow-induced vibrations[37,38]. Only a few studies have explored non-conventional configurations involving flexible plates, for example, clamped at both ends. This idea originated from efforts to harness wave energy using rubber-like elastic composite membrane structures[39]. It is evident that this configuration exhibits enhanced excitation of stable vibration modes and increased strain energy storage due to unsteady fluid effects, enabling more effective energy harvesting. Most studies focus primarily on the vibration modes and dynamic responses of clamped flexible plates. Moreover, since the natural frequency of a clamped beam is about 6 times higher than that of a cantilever beam, higher velocities are required to excite vibration modes in a clamped plate. As a result, there is limited information available regarding the FSI of clamped flexible plates, let along the effect of introducing a bluff body upstream of the clamped flexible plates and the interaction between vortex shedding and the structures. To the best of our knowledge, no studies have assessed the energy harvesting potential of clamped plates behind a bluff body or provided optimal geometric parameters for the bluff body and plate to maximize energy generation. Consequently, there is a critical need for a comprehensive study to understand the effects of geometric and flow parameters on the energy

harvesting performance of flexible plates and methods to improve their performance. To address this gap, this paper presents a computational study assessing the energy harvesting performance of clamped flexible plates influenced by vortex shedding behind bluff bodies using high-fidelity FSI simulations. The study aims to establish correlations between the size of the wake-generating bluff body, its placement, plate dimensions, material properties, and the plate's response to flow to evaluate the harvested energy.

The subsequent sections of this paper are organized as follows: in Section 2, we present the numerical algorithm used for the FSI simulations, followed by the validation studies using the Turek-Hron FSI benchmarks. In Section 3, we first describe the setup of 2D computational model for this study, and we follow it by an exhaustive analysis of the impacts of various physical parameters and the interplay between vortex shedding and the presence of plates on the fluid-induced vibration (FIV) response and energy harvesting performance. Finally, in Section 4, we present the summary and conclusions drawn from this study.

II. GOVERNING EQUATIONS, COMPUTATIONAL FRAMEWORK AND ITS VALIDATION

The fluid flow is assumed to be laminar, isothermal and incompressible, and the solid is flexible and undergoes large deformations. The Navier-Stokes equations for the flows of interest in the current work are given as

$$\rho^f \frac{\partial \mathbf{v}^f}{\partial t} + \rho^f \left(\mathbf{v}^f \cdot \nabla\right) \mathbf{v}^f - \mu^f \Delta \mathbf{v}^f + \nabla p = \mathbf{g}^f \tag{1a}$$

$$\nabla \cdot \mathbf{v}^f = 0 \tag{1b}$$

where $\mathbf{v}^f$ is the velocity of the fluid, p is the fluid pressure, ρ^f is the density of the fluid, $\mathbf{g}^f$ is the body force in the fluid domain, and μ^f is the dynamic viscosity of the fluid.

The governing equation for the dynamics of elastic structures is given as,

$$\rho^s \frac{\partial^2 \mathbf{d}^s}{\partial t^2} - \nabla \cdot \boldsymbol{\sigma}^s = \mathbf{g}^s \tag{2}$$

where ρ^s is the density of the solid, $\mathbf{d}^s$ is the displacement of the solid, $\mathbf{g}^s$ is the body force in the solid domain, $\boldsymbol{\sigma}^s$ is the Cauchy stress tensor which depends upon the type of material model.

The boundary conditions on the fluid-solid interface are given by

$$\mathbf{v}^f = \mathbf{v}^s \tag{3a}$$

$$\boldsymbol{\sigma}^f \cdot \mathbf{n}^f + \boldsymbol{\sigma}^s \cdot \mathbf{n}^s = \mathbf{0} \tag{3b}$$

where $\mathbf{n}^f$ and $\mathbf{n}^s$ are the respective unit outward normals on the boundaries of fluid and solid domains. Eq.(3a) is the kinematic constraint, which implies the no-slip condition for the flow. Eq.(3b) implies balance of tractions at the interface.

The computational framework for FSI problems employed in this work is the one based on the Cut Finite Element Method (CutFEM) proposed in Kadapa et al.[40–42]. In this framework, the fluid domain is discretized with hierarchical B-splines on fixed Cartesian grids and solved using SUPG/PSPG-stablised velocity-pressure coupled formulation. The solid problem is solved using the bi-linear finite elements. The hyperelastic material model is the Saint Venant-Kirchhoff for the validation case and Neo-Hookean for the flexible plates case. The time integration scheme used for elastodynamics is the one from Kadapa et al.[43].

The coupling between the fluid and solid domains is resolved by a second-order accurate staggered solution scheme based on Dirichlet–Neumann coupling[44], which is demonstrated to be computationally efficient, robust, and capable of handling challenging FSI problems with significant added-mass instabilities. In this coupling scheme, the fluid and structure coupling is treated in a weakly coupled way, with the fluid and solid problems being solved only once per time step. For the time integration of both fluid and solid problems, a second-order accurate generalized-α scheme is used. The flowchart of the FSI solver is shown in Fig. 1. The parameter β in Fig. 1 is defined by us as a relaxation factor[44] and can be chosen freely to optimize the rate of convergence. Large added-mass effects require the choice of a value of β close to zero. However, since the added-mass effects in the examples of this article are moderate, the chosen β does not significantly impact accuracy. The value of β we chose in this work is 0.1.

The overall FSI computational methodology adapted in this work has been validated using several benchmark examples in Kadapa et al.[40–42,45,46]. Despite its simplicity and without coupling iterations at each time step, the staggered scheme has been demonstrated to solve challenging FSI problems, including those with flexible structures for which many FSI coupling schemes either struggle to converge, thereby requiring a significant number of iterations, or completely fail[42,46]. For the details of the numerical methods, the reader is referred to Kadapa et al.[40–42,45,46].

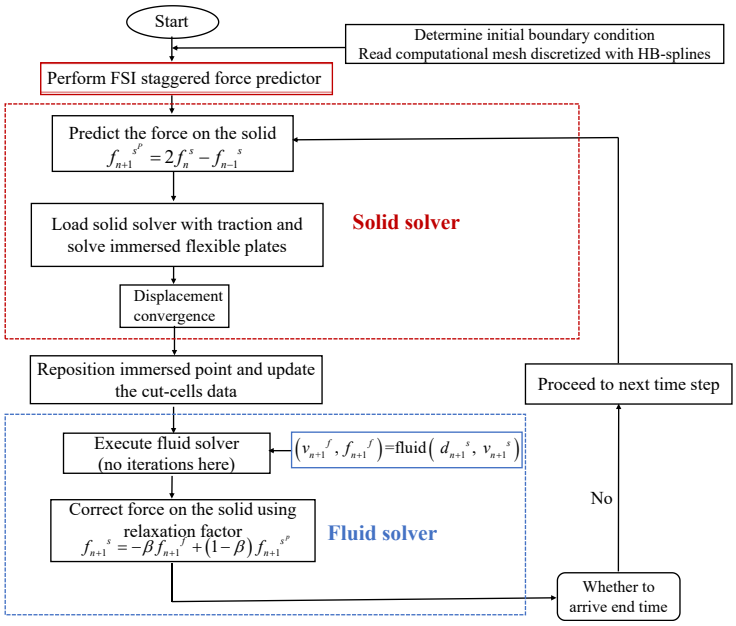

FIG. 1: Flowchart of the FSI solver.

A. Verification of the FSI framework using benchmarks

Before assessing the energy harvesting performance of two symmetric plates placed behind a bluff body, we verify the computational FSI framework used in this study by employing the well-known Turek-Hron FSI benchmarks[47]. The geometry and boundary conditions of the problem are shown in Fig.2(a). An elastic plate with a free rear end is attached to a fixed cylinder in the flow field. The inlet velocity v_{in}, illustrated in Fig.2(a), is prescribed as a parabolic profile: $v_{\text{in}} = 1.5\bar{v}\frac{4.0}{0.1681}y(0.41-y)$, where $\bar{v}$ is the average inlet velocity. The B-spline mesh with level-2 hierarchical refinement near the cylinder and the plate is shown in Fig. 2(b). An additional layer of refinement is applied for the level-3 mesh. For the test case FSI2, the fluid density and viscosity are $\rho_f = 1.0 \times 10^3$ kg m^{-3} and $\mu_f = 1.0 \times 10^{-3}$ m^2 s^{-1}, respectively; while the solid density, Young's modulus, and Poisson's ratio are $\rho_s = 10.0 \times 10^3$ kg m^{-3}, $E = 1.4$ MPa, and $\nu^s = 0.4$, respectively. In test case FSI3, the solid density and Young's modulus are $\rho_s = 1.0 \times 10^3$ kg m^{-3} and $E = 5.6$ MPa, respectively. The average inlet velocity $\bar{v}$ for the FSI2 case is 1 m/s, and for the

FSI3 case is 2 m/s.

For the spatial and temporal convergence study, simulations are performed on level-2 and level-3 meshes with different time steps: $\Delta t = 0.002$ s and $\Delta t = 0.001$ s for the FSI2 case, and $\Delta t = 0.001$ s and $\Delta t = 0.0005$ s for the FSI3 case. The vertical displacement of point A ($y_{\max}$) and the total lift (F_L) of the cylinder+flag are compared against the reference values. The numerical results for the FSI2 and FSI3 cases are tabulated in Tables I and II, respectively. The comparison of the evolution of the y-displacement of point A and the y-component of the force is shown in Figs.3 and 4, respectively, for the level-3 mesh.

As shown in Table I, the results obtained with $\Delta t = 0.001$ match well with the reference values. Table I indicates that the relative errors for level-2 and level-3 meshes are small with the same time steps. Additionally, the data in Table II shows that the relative errors for time steps $\Delta t = 0.0005$ and $\Delta t = 0.001$ are negligible. Figures 3 and 4 illustrate that the vertical displacement of point A and the lift coefficient for both cases match well with the reference results. These findings suggest that the results obtained with the current scheme converge to the reference values with mesh refinement and reduction of time step size. Considering accuracy and computational cost, the level-2 mesh refinement is sufficient to compute force coefficients and displacement responses with acceptable accuracy. This allows us to test different scenarios and a range of parameters for the problem of clamped flexible plates, which is of interest in the present work.

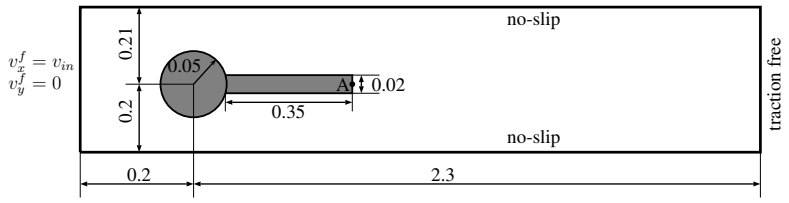

(a) Geometry and boundary conditions

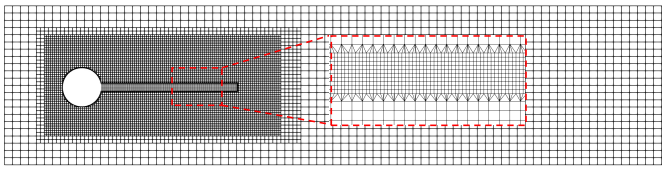

(b) Hierarchical B-spline mesh

FIG. 2: Turek-Hron benchmark problem: geometry and boundary conditions and grids of fluid and solid.

	Total DOF	$y_{\max}(\times 10^{-3})$ of A	Lift force (F_L)
Turek-Hron[47]-Level-2, $\Delta t = 0.001$	19488	1.18 ± 78.80	0.80 ± 286.0
Turek-Hron[47]-Level-3, $\Delta t = 0.001$	76672	1.25 ± 79.3	0.41 ± 229.3
Present-Level-2, $\Delta t = 0.002$	26565	1.32 ± 74.31	0.17 ± 233.39
Present-Level-3, $\Delta t = 0.002$	70068	1.21 ± 77.11	1.73 ± 230.19
Present-Level-2, $\Delta t = 0.001$	26565	1.30 ± 78.61	1.67 ± 234.93
Present-Level-3, $\Delta t = 0.001$	70068	1.18 ± 80.56	0.10 ± 230.06

TABLE I: Turek-Hron FSI2 case: vertical displacement ($y_{\max}$) of point A and total lift force (F_L) on the cylinder+flag for different levels of meshes and time steps.

	Total DOF	$y_{\max}(\times 10^{-3})$ of A	Lift force F_L
Turek-Hron[47]-Level-2, $\Delta t = 0.0005$	19488	1.19 ± 35.72	8.26 ± 163.72
Turek-Hron[47]-Level-3, $\Delta t = 0.0005$	76672	1.45 ± 35.34	1.42 ± 146.43
Present-Level-2, $\Delta t = 0.001$	26565	1.31 ± 37.41	2.41 ± 138.88
Present-Level-3, $\Delta t = 0.001$	70068	1.24 ± 36.12	2.34 ± 145.76
Present-Level-2, $\Delta t = 0.0005$	26565	1.17 ± 37.21	1.76 ± 141.37
Present-Level-3, $\Delta t = 0.0005$	70068	1.46 ± 35.63	1.58 ± 146.34

TABLE II: Turek-Hron FSI3 case: vertical displacement ($y_{\max}$) of point A and total lift force (F_L) of the cylinder+flag for different levels of meshes and time steps.

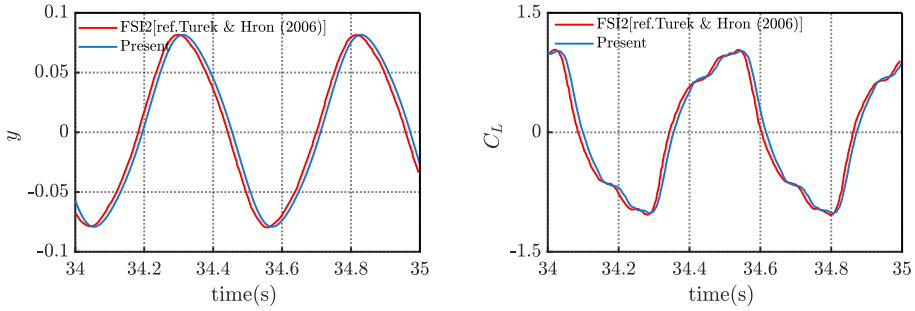

(a) (b)

FIG. 3: Turek-Hron FSI2 case: comparison of results obtained with Level-3 mesh and $\Delta t = 0.001$ against the reference: (a) displacement versus time of point A, (b) lift coefficient of the cylinder+flag versus time.

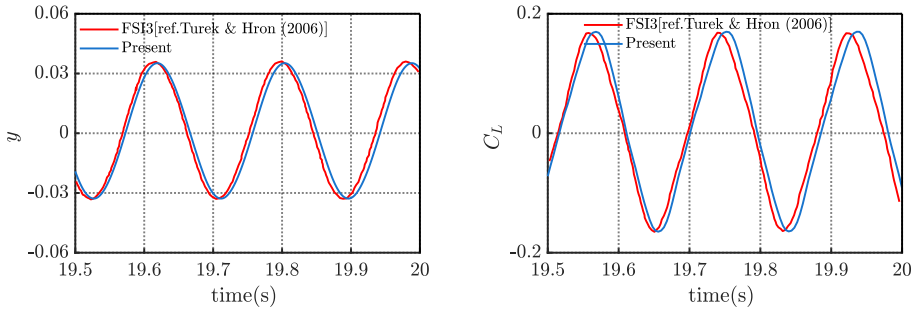

FIG. 4: Turek-Hron FSI3 case: comparison of results obtained with Level-3 mesh and $\Delta t = 0.0005$ against the reference: (a) displacement versus time of point A, (b) lift coefficient of the cylinder+flag versus time.

III. PROBLEM SETUP, RESULTS AND DISCUSSION

A. Set up of the problem

The system considered in this work consists of two flexible plates clamped at both ends. These plates are situated parallel to each other and the flow. The domain measures 6×4 m^2. As illustrated in Fig.5(a), L and H represent the length and width of the plates, respectively. The leading edges of the plates are positioned 1 m from the inlet. A square bluff body with length l and width h is strategically placed between the two flexible plates. The overall configuration is shown in Fig.5(a). The B-spline mesh with a level-2 hierarchical refinement of the fluid domain is depicted in Fig. 5(b). Starting with a 121 × 51 element grid, the coarsest element size measures 0.03306 m × 0.01961 m, while the finest element size measures 0.00826 m × 0.00490 m. The solid mesh for the plates is discretised with a 50 × 4 mesh. Based on the results from the Turek-Hron FSI2 and FSI3 cases, a constant uniform time step of $\Delta t = 0.001$ is employed for the simulations. A uniform velocity v_{in} is imposed at the inlet in the X-direction. The fluid density is $\rho_f = 10^3$ kg m^{-3}, and its dynamic viscosity is $\mu_f = 0.001$ m^2 s^{-1}. The density of the solid is $\rho_s = 10 \times 10^3$ kg m^{-3}, with Young's modulus $E = 14$ MPa and Poisson's ratio $\nu = 0.4$.

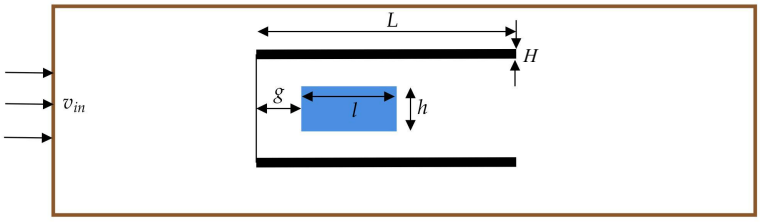

(a) Problem setup

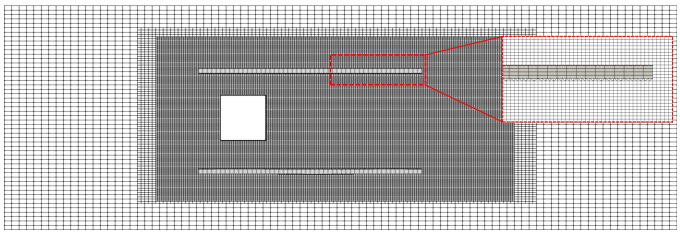

(b) Hierarchical B-spline mesh for the fluid domain

FIG. 5: FSI model: problem setup and mesh of fluid and solid.

The energy harvesting performance in this study is evaluated by calculating the total strain energy of each plate. The elastic strain energy is defined as,

$$E_s = \int_\Omega \frac{1}{2} \mathbf{L}^T \mathbf{S} \, dV \tag{4}$$

where $\mathbf{S}$ is second Piola-Kirchhoff stress tensor and $\mathbf{L}$ is Green-Lagrange strain tensor.

The elastic strain energy is computed at each time step for each plate and is further postprocessed to calculate time-averaged values as

$$\overline{E}_s = \frac{1}{T_t} \int_{t_0}^{t_0+T_t} E_s(t) \, dt \tag{5}$$

where t_0 is the starting time instant from which the average is calculated, and T_t is the time duration considered. Based on the preliminary results obtained, we chose $t_0 = 10$ s as it gives ample time for the initial transient responses to die down. The simulations are performed for a total duration of 60 s; therefore, $T_t = 50$ s. The Reynolds number is calculated as $Re = \rho^f v_{in} h / \mu^f$.

B. Effect of the bluff body on the response of the plates

Numerical studies are conducted to investigate the effect of a bluff body on the dynamics of two parallel plates and characterise the effect of the bluff body on their energy harvesting performance. The first set of studies involve configurations of two parallel clamped plates without and with a square body positioned in the center. Simulations are performed for different *Re* values in the range of 100 and 600. The size of the bluff body is 0.2×0.2 m^2, and g is 0.4 m.

Fig. 6 depicts contours of vorticity and graphs of $\overline{E}_s$ for three different *Re* values for the cases without and with a bluff body. For all the cases of *Re* considered, the values of $\overline{E}_s$ are higher for the case with a bluff body than compared with the case with plates only. As shown, introducing a bluff body increases the displacement magnitude and, hence, $\overline{E}_s$ through the mechanism of vortex shedding behind bluff bodies.

Figure 7(a) shows the sum of the mean strain energy of the two plates with and without a bluff body for different Reynolds numbers (*Re*). It can be observed that $\overline{E}_s$ for the plates with a bluff body increases, and the differences in $\overline{E}_s$ between the two configurations grow with the Reynolds number. The trend of the displacement of the midpoint $\bar{y}_n$ on the lower surface of the upper plate versus *Re* in Fig.7(b) exhibits similarities to the strain energy trend illustrated in Fig.7(a). This demonstrates that the presence of the bluff body contributes to higher energy output due to increased deformation of the plates. The introduction of the bluff body generates vortices that alternately detach from the bluff body and the trailing edge of the plate. These alternating shedding vortices transport flow kinetic energy to the structure by inducing vibrations in the two parallel plates. As shown in Fig.6, the strain energy E_s of the plates in configurations with a bluff body exhibits periodic oscillations due to the periodic deformation of the plates induced by vortex shedding. Furthermore, Fig.6 shows that the vortical structures exhibit greater strength, which corresponds with the higher strain energy generated by the plates as *Re* increases. It is worth noting that alternating vortices are shed from the trailing edge of the two plates in the configuration without the bluff body at $Re = 500$. The phenomenon where $\overline{E}_s$ reaches a maximum at $Re = 500$, as shown in Fig. 7, can be better explained by the synchronization of vortex shedding and plate oscillation.

The results indicate that the placement of a bluff body significantly enhances the strain energy of the structure due to vortex shedding behind the bluff body, which intensifies the interaction between the fluid and the plates. Therefore, it is crucial to determine the optimal design parameters

of the bluff body and the plates to maximize strain energy and effectively convert it into electrical energy. In the following sections, we study the effects of the bluff body's location and geometry, as well as the aspect ratio and Young's modulus of the plates. We also discuss the deformation of the plates, the flow field, and the energy harvesting performance.

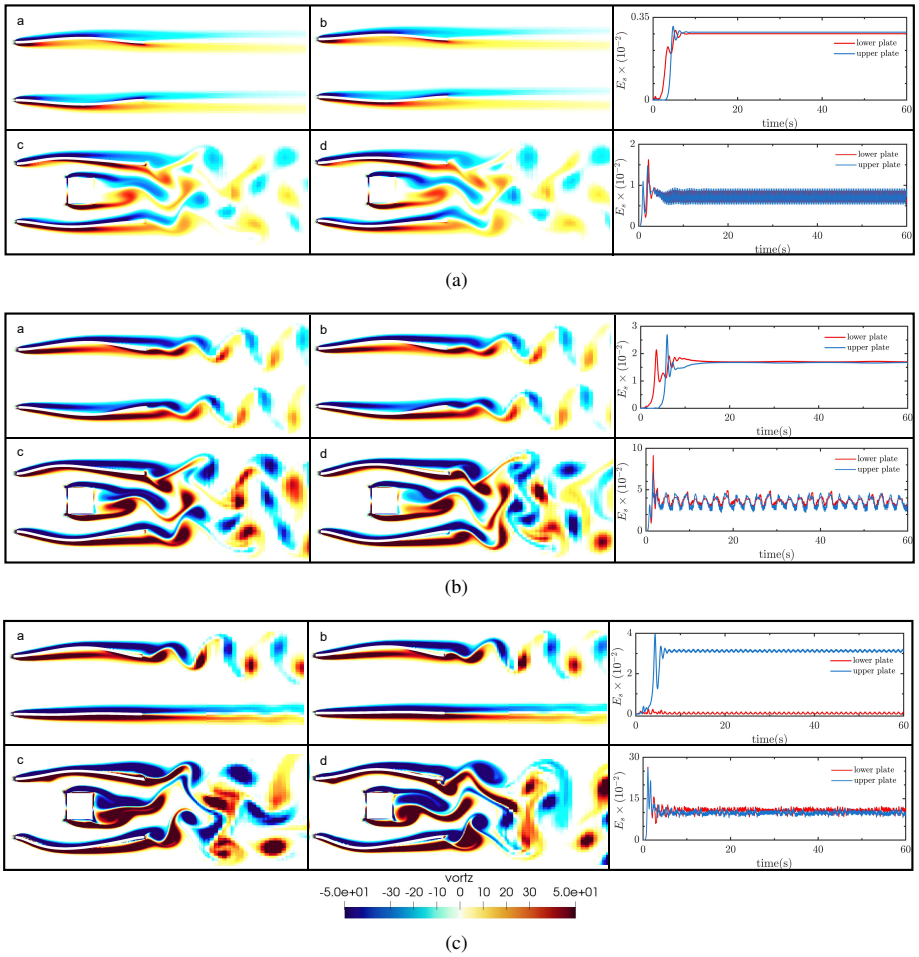

(a)

(b)

(c)

FIG. 6: Contours of vorticity at different Re and time of configurations with and without a bluff body along with strain energy E_s versus time: (a) $Re = 300$, (b) $Re = 500$, (c) $Re = 600$ at $t = 52.6$ s and at $t = 54.2$ s.

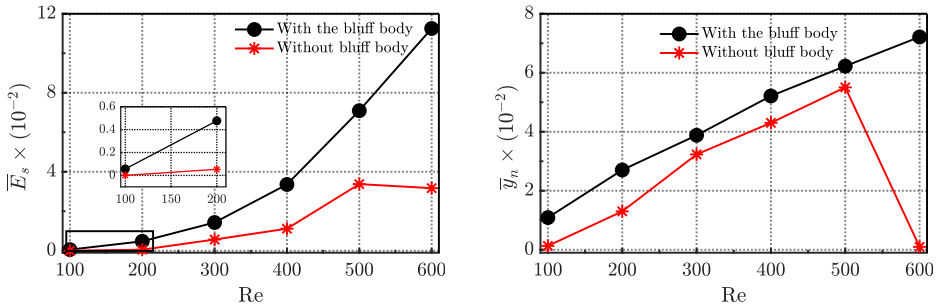

FIG. 7: Energy and displacement of configurations with and without a bluff body versus different Re: (a) the sum of strain energy $\overline{E}_s$ of two plates, (b) displacement $\overline{y}_n$ of the midpoint on the lower surface of the upper plate.

1. Location of the bluff body for optimal performance

As alternating vortices with varying sizes and frequencies are continuously shed from the bluff body, its geometry and placement can significantly influence the response characteristics and deformation behavior of the plates. Therefore, we first determine the optimal location of the bluff body while keeping the aspect ratio $l/h = 1.0$ fixed for all simulation cases in this part.

For a fixed geometric configuration of the body, both *Re* and location g are varied, and the mean strain energy $\overline{E}_s$ is evaluated, as depicted in Fig. 8. It can be observed that a higher Reynolds number leads to higher energy harvesting performance, as expected. Notably, at a given *Re*, the average strain energy $\overline{E}_s$ reaches its minimum when the g is 0.2, subsequently rising with the increase of g. Moreover, this suggests diminishing effects on fluid flow across the plates when the bluff body is located at the midsection or leading edge. This leads to a comparatively modest deformation of the plates at these specific locations. Slight differences in the energies of the lower and upper plates can be attributed to the asymmetric nature of complex vortex shedding in many cases. Overall, we notice that the location of the bluff body significantly influences the energy harvesting performance, with the amount of strain energy increasing as the bluff body is moved toward the trailing edge of the plates.

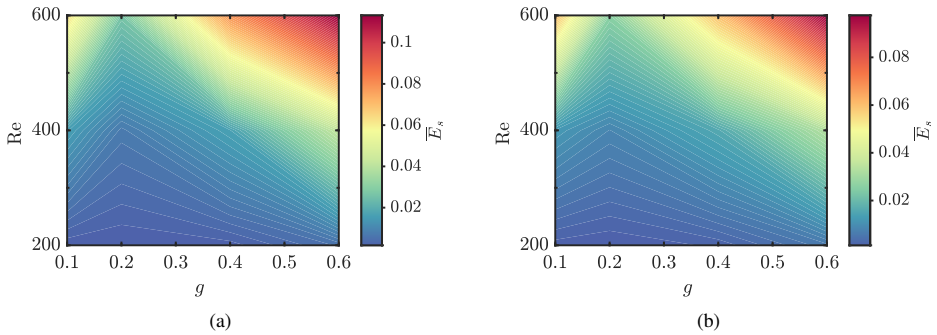

FIG. 8: Contours of mean strain energy $\overline{E}_s$ by varying Reynolds number and g: (a) the upper plate, (b) the lower plate.

To investigate the influence of the location of a bluff body on the behaviour of the structure, the frequency correlations among the flow field around the structure, vibration of the structure, and vortices shed from the bluff body at $Re = 400$ are shown in Fig. 9. The normalized lift coefficient C_f of the fixed bluff body, the vertical displacement fluctuation $y - \overline{y}$ of the lower plate, and the fluctuation of lift coefficient $C_L - \overline{C}_L$ of the lower plate are taken as the signals adopted by Fast Fourier transform (FFT). The frequency spectrum shown in Figs. 9(a)- 9(d) include multiple frequencies of the lift coefficient and spectral noise (the signal has been denoised). These reveal that the shedding vortices and the vibration of the plate have no clear regularity and periodicity as the bluff body is placed at $g = 0.1$ and $g = 0.2$. The dominant frequency in the flow is attributed to the convection and successive shedding of leading-edge vortices coupled with the vibration of the plate. As shown in Figs. 9(e) and 9(f), the flow field around the bluff body and the plate exhibit a distinct dominant frequency of $f = 3.418$ Hz, *which indicates a fully synchronised state for this combination of parameters*. The phenomenon that better energy harvesting performance obtained at $g = 0.6$ in Fig. 8 can be better explained by the fact that *the alternate shedding of a pair of vortices from both ends of the bluff body and plate synchronize well with the plate's vibration.*

To better clarify the interaction between the bluff body and plate, instantaneous vorticity patterns with varying location g for the whole configuration, along with the lift coefficient of the bluff body C_f and the lift coefficient of the whole upper plate C_L are illustrated in Fig. 10. As depicted in Fig. 10(a) and 10(b), it is apparent that the generation and detachment of vortices exhibit highly nonlinear dynamic behaviour, attributed to the more intricate interaction involving vortices gen-

erated from the tail end between the bluff body and the two plates. These irregularities observed in the formation and shedding of vortices validate the presence of spectral noise, as depicted in Fig. 9(a)- 9(d). Moreover, Fig.10(b) suggests an approximate inverse relationship between the lift coefficients C_f and C_L, indicating that when C_f reaches its local peak, C_L correspondingly reaches its minimum. Furthermore, in Fig. 10(a), we observe opposing vortices, characterized as positive and negative, shedding along the upper and lower surfaces of the plate from the trailing edge. The formation of these positive and negative vortices induces periodic variations in the pressure distribution on the upper and lower surfaces of the plate, leading to increased lift force fluctuations. We observe alternate shedding of a pair of vortices within a transverse oscillation cycle occurs as shown in Fig. 10(c). Moreover, Fig. 9 reveals a single peak in the vibration at $g = 0.6$, whereas the vibrations at $g = 0.1$ and $g = 0.2$ exhibit multiple peaks, indicating a clear synchronisation of vortex shedding and plate oscillations.

The instantaneous pressure is explored alongside vortex evolution to further explain the structural deformation, taking the configuration of $g = 0.1$ as a case study. The vorticity with streamline patterns and the upper surface pressure coefficients are given in Fig. 11. At $g = 0.1$, the response exhibits non-periodic behaviour. In Fig. 9(b), another peak closely follows the dominant frequency peak, and these high-frequency peaks can be explained by the evolution of vortex structures shown in Fig. 11. At $t = 35.8$ s, there are two clockwise vortices on the upper surface of the plate, denoted as A and B, which cause two low-pressure vortex core regions. This is reflected as two distinct peaks in the distribution of transient upper surface pressure shown in Fig. 11. From $t = 35.8$ s to $t = 35.9$ s, vortices A and B move downstream, leading to the downstream movement of the peaks illustrated in the curve. At $t = 36.0$ s, vortex B sheds from the tail end, and the small vortex C forms and gradually strengthens.

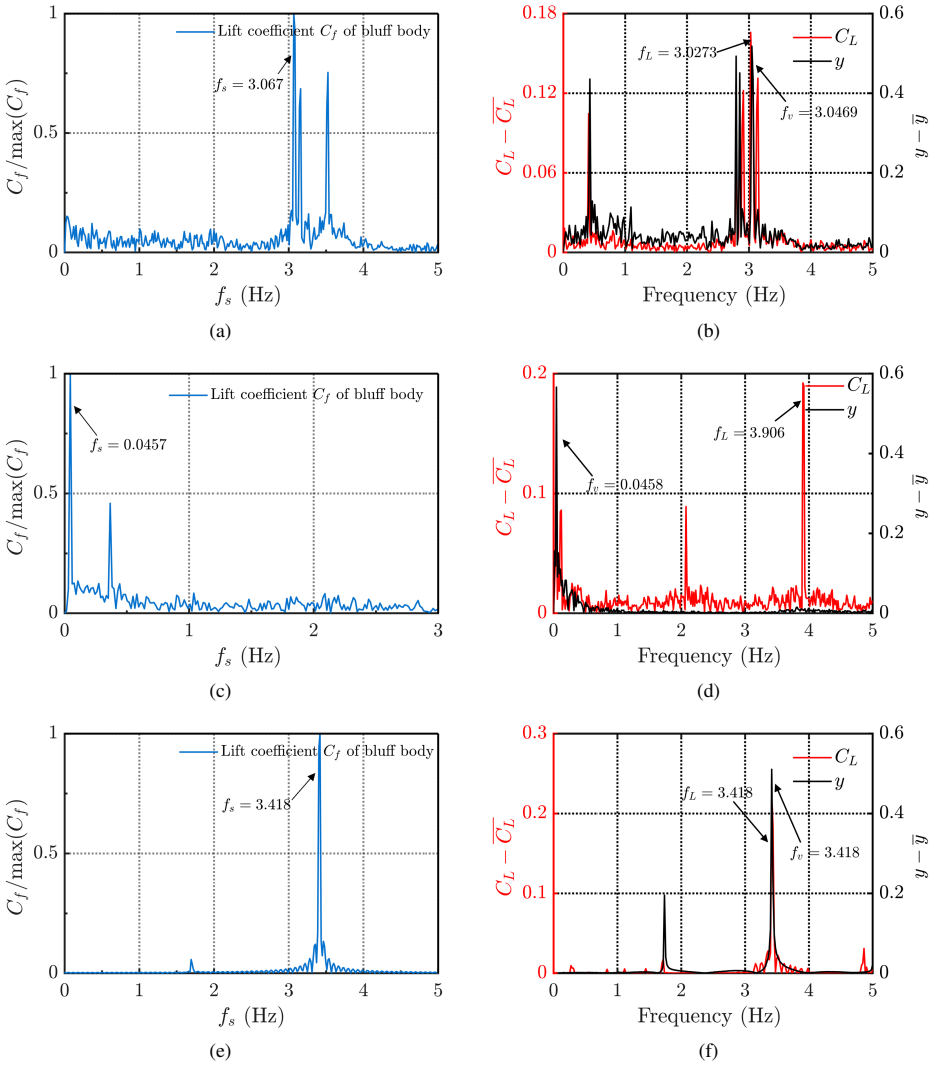

FIG. 9: Frequency characteristics of bluff body at $Re = 400$: (a) $g = 0.1$,(c) $g = 0.2$, (e) $g = 0.6$ and plate structure: (b) $g = 0.1$,(d) $g = 0.2$, (f) $g = 0.6$.

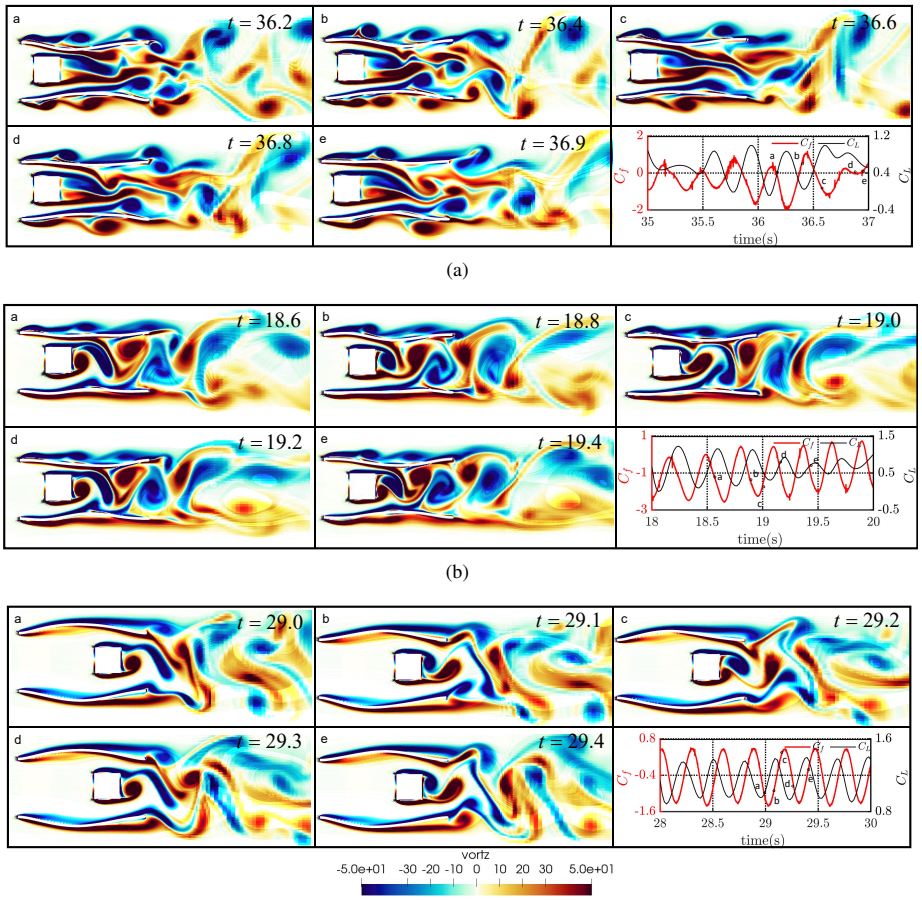

FIG. 10: Contours of vorticity at different location g and lift coefficient C_f of bluff body versus time: (a) $g = 0.1$, (b) $g = 0.2$, (c) $g = 0.6$.

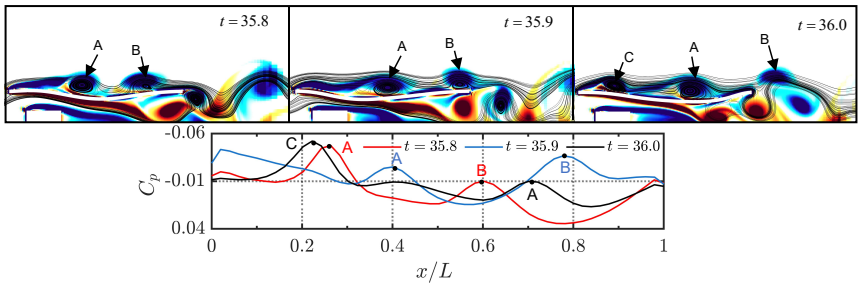

FIG. 11: Transient vorticity with streamline patterns at $g = 0.1$.

2. *Effect of the geometry of the bluff body*

After determining the optimal location g, in this section, we studied the effect of the geometry of the bluff body on energy harvesting performance. Simulations are performed over different aspect ratios l/h of the bluff body, ranging from 0.5 to 3.0 ($0.1 \leq l \leq 0.4$, $0.1 \leq h \leq 0.3$) under $g = 0.6$ and $L/H = 50$ at $Re = 400$. The mean strain energy $\overline{E}_s$ under different l/h ratios is shown in Fig. 12. We observe that the energy harvesting performance at $h = 0.1$ is better than that of the other geometric configurations of the bluff body, especially for $l \leq 0.3$. This can be explained by the fact that increased inlet velocity v_{in} at $h = 0.1$ at fixed $Re = 400$ consequently results in an amplified pressure difference between the upper and lower surfaces of the plates. Additionally, it enhances the interfering effects of detached vortices on the flow field, thereby inducing significant deformation.

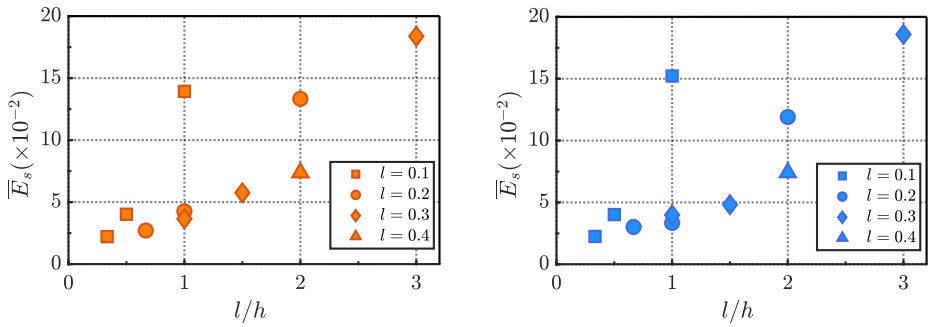

FIG. 12: Mean strain energy $\overline{E}_s$ versus different l/h ratios of the bluff body: (a) lower plate, (b) upper plate.

To better understand the features of the flow field, structure, and energy field at different l/h, the characteristics of the time domain for different physical fields are further explored. For the results discussed in III B 1, the bluff body aspect ratios of 0.5, 1, 2, and 3 at the location $g = 0.6$ were selected as typical cases for this part. Fig. 13 illustrates the time evolutions of the lift coefficient of the bluff body (C_f) and the whole plate (C_L), the strain energy (E_s), and the spatial average plate vibration $\overline{y}$ for the selected l/h of the lower plate. In this context, the most important observations are as follows: It can be noted that all the physical fields exhibit oscillatory characteristics with periodicity and display oscillations at the same frequency when $h = 0.2$ with $l = 0.1$ and $l = 0.2$ as shown in Fig. 13(b) and 13(e). In other cases, the response of all the physical fields is non-periodic. We suspect that higher velocities of flow lead to more significant and irregular vibration and mean hydrodynamic performance. This non-periodic behavior signifies complex interactions between the fluid and structures (plates). Furthermore, the mean lift coefficient values (C_f) of the bluff body exhibit a deviation from zero, indicating an asymmetrical vortex detachment that leads to an imbalanced pressure distribution. This explains the fact that there exist some differences in the mean strain energy values between the upper and lower plates, as shown in Fig. 12. It is also worth noting that the mean vertical displacement of vibration and the variation in strain energy are synchronized over time for all cases, as depicted in Fig. 13. This synchronization signifies that when displacement reaches its peak, strain energy correspondingly reaches its maximum.

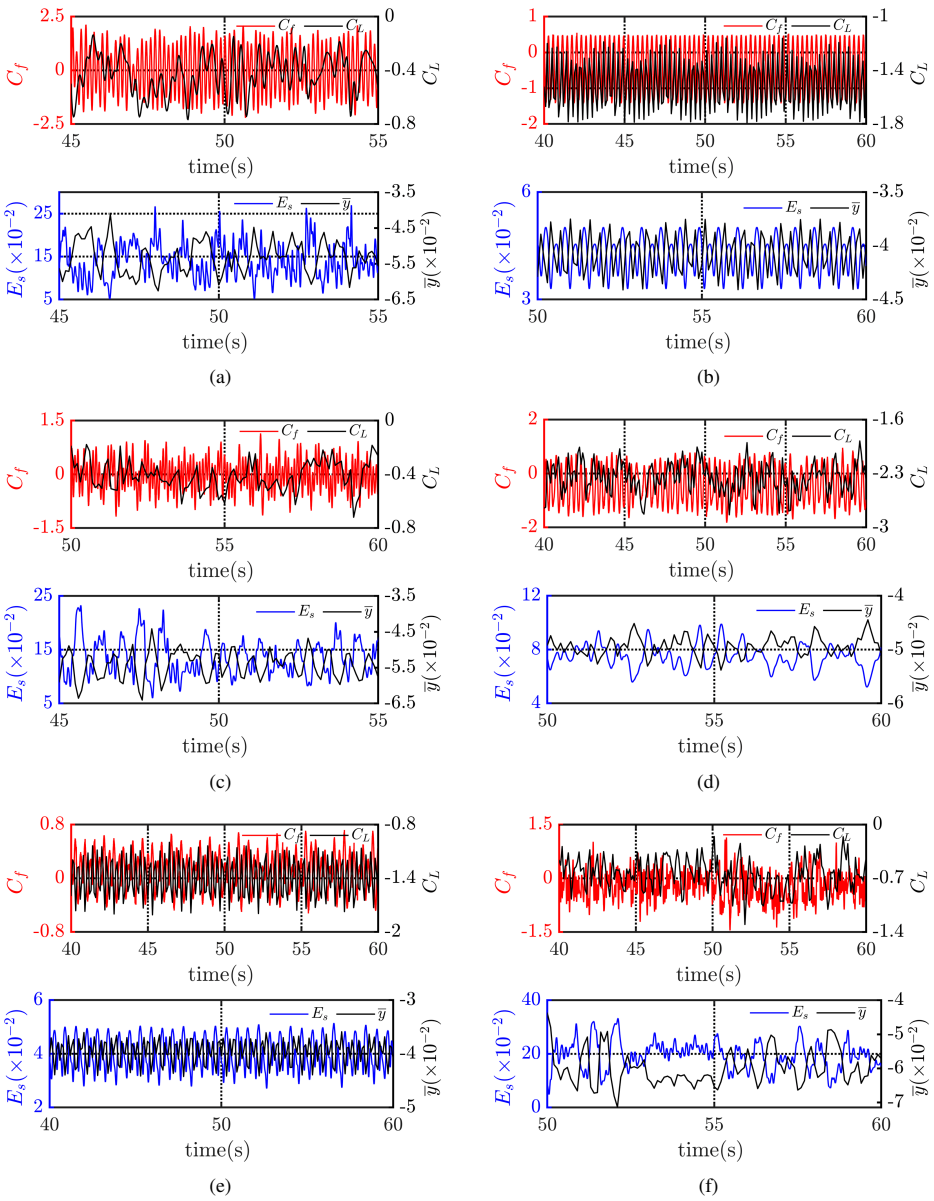

FIG. 13: Time histories of lift coefficients (C_f and C_L), and the strain energy E_s, and mean plate displacement $\overline{y}$ at (a) $l = 0.1$, $h = 0.1$, (b) $l = 0.2$, $h = 0.2$, (c) $l = 0.2$, $h = 0.1$, (d) $l = 0.4$, $h = 0.2$, (e) $l = 0.1$, $h = 0.2$, and (f) $l = 0.3$, $h = 0.1$.

In addition to the temporal mean characteristics, the vibration characteristics of the plate structure and the characteristics of the flow field around the plate in the spatial domain are also of interest. The spatial distribution along the x-axis of the mean displacement $y^{'}$ and the average total lift $\overline{C}_L$ experienced by the upper and lower surfaces when the global field achieves stable response are presented in Fig. 14, respectively. We observe the first mode standing wave response of the plate in Fig. 14(a), indicating that the geometry of the bluff body has no obvious influence on the vibration mode of the plate. With the mean characteristics of structure response changing, the mean hydrodynamic performance is changed, as shown in Fig. 14(b). The distribution characteristics of deformation are essentially consistent with the distribution characteristics of lift. It is clear that the change in the height h of the bluff body results in the variation of different hydrodynamic effects near the plate. Specifically, for the three cases at $h = 0.1$, lift distribution along the X-axis shows similar trends. Likewise, at $h = 0.2$, lift distribution along the X-axis also displays comparable characteristics. This impact greatly influences the deformation of the structure, thereby affecting the energy harvesting performance. Furthermore, it is noteworthy that, for $h = 0.2$, the observed deformation distributions are relatively smaller in comparison to those associated with the bluff body shape of $h = 0.1$. This phenomenon is consistent with the variation in mean strain energy $\overline{E}_s$ depicted in Fig. 12.

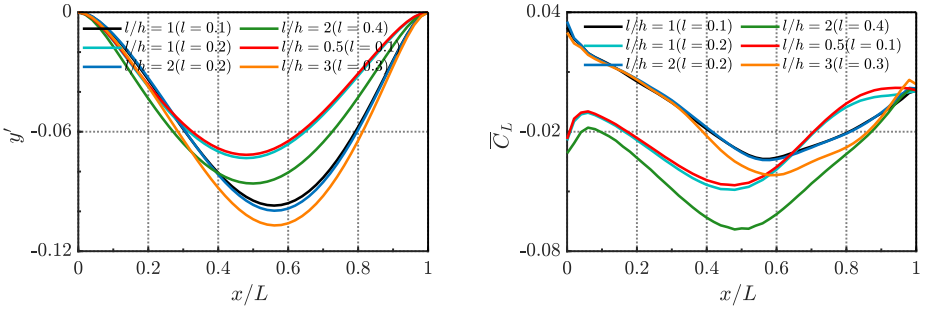

FIG. 14: Mean (a) deformation and (b) surface lift coefficient along the plate in the different l/h.

The vortex evolution and frequency of the structure are concerned in Fig. 15 to further explain the interaction between the flow and structure. Here, t^* is defined as t/T, where T is the period of the wake-shedding frequency of the bluff body. It can be observed that bluff bodies with $h = 0.1$ depicted in Fig. 15(a) and (b) have the potential to induce significant flow disturbances, resulting in

a more complex and irregular flow pattern as fluid traverses the structure compared to the patterns shown in Fig. 15(c) and (d). Additionally, in Fig. 15(a) and (b), the wake pattern illustrates the formation and shedding of several strong clockwise and counterclockwise vortices along the upper and lower surfaces, respectively. Furthermore, from the frequency characteristics of the flow field, we can observe that at $h = 0.1$, the response of the flow field is non-periodic. In Fig. 15(a) and (b), the flow field around the bluff body and the lower plate have the same peak frequencies of $f = 7.019$Hz and $f = 10.071$Hz, respectively. Additionally, these two frequencies appear as dominant in the flow field of the lower plate. The dominant frequencies of lift fluctuation on the plate, as depicted in Fig. 15(a) and (b), are $f = 0.305$Hz and $f = 0.458$Hz, respectively. We can see that several peaks exist in the vicinity of the dominant frequency peak in Fig. 15(a) and (b). Considering their presented wake patterns, the high-frequency peaks observed can be attributed to the evolution of vortex structures along the plate's surface. Specifically, the surface of the structure exhibits two or three vortices. Moreover, in Fig. 15(d), the flow field around both the bluff body and the lower plate exhibits a dominant frequency of $f = 3.159$Hz, which suggests *a synchronised response between the flow field and the plates* for these parameters. This can be explained by the fact that a pair of vortices detach respectively from the trailing edge of the plate and the rear of the bluff body.

We have discussed the evolution of vortices and the frequency characteristics of the flow field above. Fig. 16 plots the vorticity and streaming patterns at three typical instants, along with the corresponding surface pressure coefficients on the upper surface of the lower plate, considering $l/h = 0.3$ as a typical case. In Fig. 16, from $t = 40.0$s to $t = 40.2$s, there are several local low-pressure regions because of the existence of vortices along the plate. Accordingly, there are a corresponding number of distinct peaks in the distribution of transient upper surface pressure along the plate. Based on the discussion above, for a fixed Reynolds number of 400 and $h = 0.1$ of the bluff body, the flow instability induces vortex formation and shedding, causing non-uniform pressure distribution. Combining spectral analysis from Fig. 15, the flow fields around bluff bodies and flexible plates exhibit coupled characteristics, thereby enhancing plate deformation. To sum up, it is recommended that for energy harvesting, the bluff body can be fixed at $l/h = 0.3\,(l = 0.3, h = 0.1)$ as it gives high strain energy (E_s).

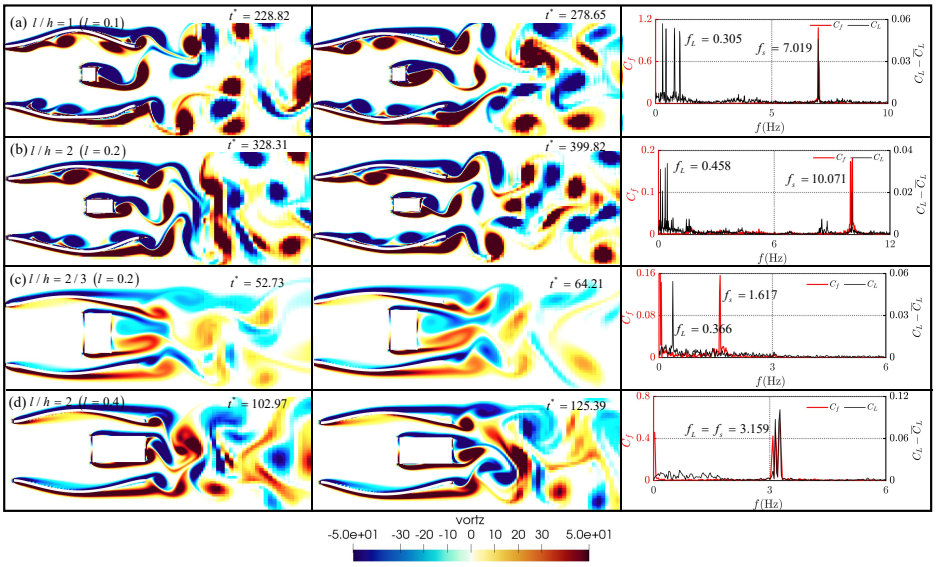

FIG. 15: Contours of vorticity at different aspect ratio l/h and frequency spectrum of lift coefficient C_f of bluff body : (a) $l/h = 1$, (b) $l/h = 2$, (c) $l/h = 2/3$, (d) $l/h = 0.2$

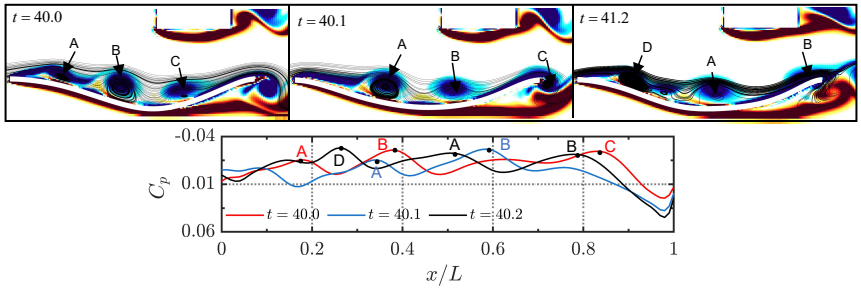

FIG. 16: Transient vorticity with streamline patterns at $l/h = 3\,(l = 0.3)$.

3. *Effect of the aspect ratio of the plate on energy harvesting*

In this section, we investigate the influence of the aspect ratio L/H of the plate on energy harvesting. The aspect ratio L/H is varied from 30 to 120 with $0.9 \leq L \leq 1.5$ and $0.01 \leq H \leq 0.03$ along with $l/h = 3$ and $g = 0.6$ for a fixed $Re = 400$. Detailed information on different cases considered, and the results obtained are presented in Table. III, showcasing variations in the mean

strain energy values of the lower plate ($\overline{E}s_1$) and upper plate ($\overline{E}s_2$). Additionally, the mean plate displacement $y_{\mathrm{m}}^{'}$ of the lower plate at the position of maximum vibration amplitude and the mean total lift coefficient $\overline{C}_L$ of the lower plate are examined in relation to the varying aspect ratio L/H of the flexible plate. From Table. III, we note that when L remains constant, and H exceeds 0.02, the strain energy of the plate decreases with increasing H. Additionally, for L ranging from 1.0 to 1.2, as H increases, both the strain energy and $y_{\mathrm{m}}^{'}$ reach a local maximum at $H = 0.02$, followed by a decrease with further increments in H. In addition, when H remains constant, the strain energy decreases with an increasing L, which indicates an inverse correlation between strain energy and L. Moreover, It can be observed that when $H = 0.01$ or $L = 1.5$, the response of all physical fields drops sharply due to the nearly negligible mean lift coefficient. This reflects that the energy harvesting performance of a flexible plate decreases with aspect ratio, especially at $30 \leq L/H \leq 75$, for a fixed value of Young's modulus and Reynolds number.

TABLE III: The value of the mean strain energy against aspect ratio L/H of the flexible plate.

L	H	L/H	$\overline{E}_{s1} \times 10^2$	$\overline{E}_{s2} \times 10^2$	$\lvert y_{\mathrm{m}}^{'} \rvert \times 10^2$	$\lvert \overline{C}_L \rvert \times 10^2$	R
0.9	0.020	45	20.8886	19.8603	10.3162	116.74	0.2308
0.9	0.025	36	18.6632	17.5580	9.4030	114.95	0.2062
0.9	0.030	30	16.7319	16.2534	8.5013	109.67	0.1849
1.0	0.010	100	0.4567	0.7918	3.9540	3.71	0.0050
1.0	0.015	66.67	16.0995	16.6058	11.3124	55.91	0.1779
1.0	0.020	50	18.3793	18.5833	10.7063	70.15	0.2031
1.0	0.025	40	17.7789	17.2075	10.0774	79.80	0.1965
1.0	0.030	33.33	17.1324	15.2070	9.3947	85.28	0.1893
1.1	0.010	110	0.3284	0.4767	3.8223	2.41	0.0036
1.1	0.015	73.33	12.1435	12.7216	10.7699	27.36	0.1342
1.1	0.020	55	15.9917	15.7503	10.6936	41.27	0.1767
1.1	0.025	44	15.6990	13.8477	10.4340	50.23	0.1735
1.1	0.030	36.67	15.7255	14.1151	9.9674	58.44	0.1738
1.2	0.010	120	0.9477	0.5875	3.5916	1.08	0.0105
1.2	0.015	80	1.9525	14.0203	3.3659	6.22	0.0216
1.2	0.020	60	2.0597	13.3185	4.8379	9.43	0.0228
1.2	0.025	48	13.1065	12.9425	10.2153	28.66	0.1488
1.2	0.030	40	13.6888	11.6699	10.1401	35.83	0.1513
1.5	0.020	75	4.4274	4.0759	5.5576	6.75	0.0489
1.5	0.025	60	4.1931	4.4686	6.2745	12.82	0.0463
1.5	0.030	50	2.7350	3.1295	5.6993	10.51	0.0302

According to Table III, the flexible structure with $L/H = 45$, which experiences a large mean lift coefficient, provides the greatest energy harvesting performance. Generally, L/H ratio has a significant influence on both $\overline{E}_s$ and $\overline{C}_L$. Fig. 17 presents the mean deformation and surface lift coefficient along the plate in the different L/H ratios we chose. According to the strain energy shown in Table. III and Fig. 17, strain energy could be maximized by the increasing deformation and lift on the surface. From Fig. 17, it is clear that both the lift response and vibration of the flexible plate can be classified into two categories based on L. Specifically, when $0.9 \leq L \leq 1.1$, the position of maximum displacement moves further from the leading edge with the increment of L. Furthermore, in Fig. 17(b), when $1.2 \leq L \leq 1.5$, we can observe that the total lift experienced by the plate is positive at the midsection of the flexible plate, which explains the upward trend in displacement observed at the midsection of the plate in Fig. 17(a). The local strain energy $\overline{E}_s^{'}$ and a normalised integral of the local strain energy $(\int_0^x \overline{E}_s^{'} dx)/\overline{E}_s$ along the x-coordinate are illustrated in Fig. 18. The local strain energy is maximized at the clamped end of the plate, especially at the trailing edge. The local strain energy between $x/L = 0.1$ and $x/L = 0.9$ is approximately a quarter of the maximum local strain energy. Furthermore, the curve of the normalised integral of the local strain energy exhibits nearly linear variation between $x/L = 0.1$ and $x/L = 0.9$. While the magnitude of local strain energy is influenced by the L/H, as depicted in Fig. 18, the global distribution characteristics of local strain energy demonstrate limited sensitivity to variations in aspect ratios. Fig. 18 suggests that the piezoelectric patches are recommended to be attached as closely as possible to the two clamped ends, where the local strain energy attains its maximum value.

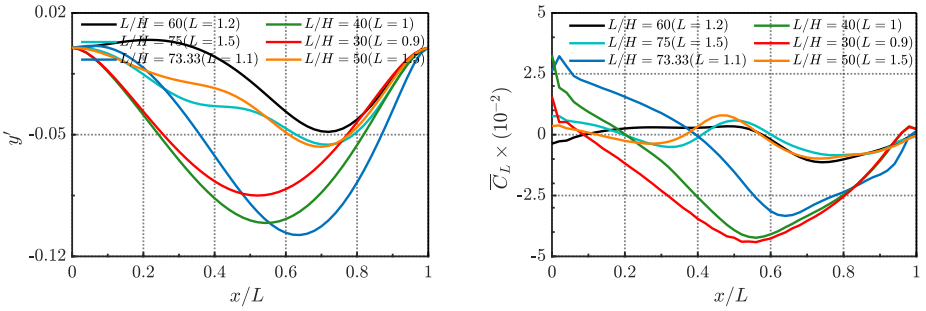

FIG. 17: Mean (a) deformation and (b) surface lift coefficient along the plate in the different L/H.

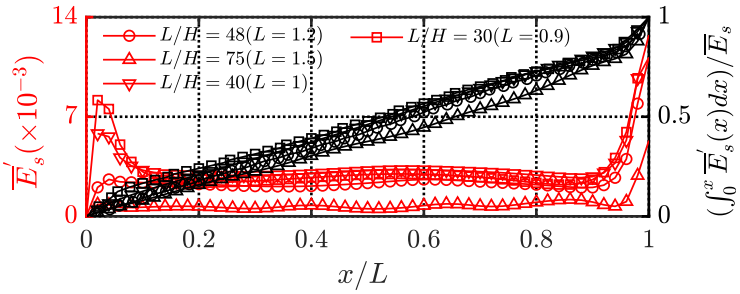

FIG. 18: Local strain energy $\overline{E}_s^{'}$ and integral of local energy along the x-coordinate of the lower plate at different L/H

We utilize a conversion ratio R defined as $R = \overline{E}_s/E_k$, as proposed by Kim et al. [38], to evaluate the efficiencies of energy harvesting systems. Here, $E_k = 1/2\rho_f U_\infty^3 \left|y_m^{'}\right|$ is the mean kinetic energy of the uniform flow. The specific values of the energy conversion efficiency with respect to L and H are illustrated in Table. III. Fig. 19 depicts the variation of energy ratio R, where the colour of the scatter represents the value of the conversion ratio of strain energy. We can observe that when L/H exceeds 100, the conversion ratio drops sharply. For any value of H within the range of 0.015 to 0.03, the trend in R remains consistent, indicating a gradual decrease in energy ratio with increasing plate length L. Additionally, from Fig. 19, we note that the conversion ratio (R) is more sensitive to variations in length L when compared with variations in thickness H. According to all the cases shown in Table. III and Fig. 19, it attains the peak strain energy and demonstrates the highest energy conversion efficiency when L/H is 45.

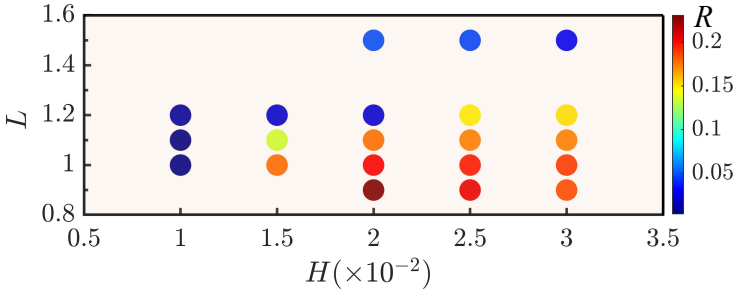

FIG. 19: The energy conversion ratio R at different L and H.

The wake pattern, pressure contours, and associated pressure coefficient C_p distribution along

the lower plate surface at two instants in time t are shown in Fig. 20, where the flow structure is depicted with streamlines indicated by black arrows. For the case at $L/H = 30$, the plate response shows the first mode standing wave response referred to in Section III B 1 seen in Fig. 20(a). For the plate with $L/H = 30$, the blue region depicted in the C_p distribution plot indicates that both the upper and lower surfaces have a downward direction of C_p, leading to a larger negative lift. Furthermore, at $t = 40$s, a weak clockwise vortex exists on the upper surface of the plate, which contributes to a local low-pressure region shown in the C_p distribution plot. It can be observed from Fig. 20(b) that, initially, at $t = 15.7$s, there are two strong clockwise vortices on the upper surface, reflected as two suction peaks in the transient upper surface pressure coefficient distribution. Consequently, we can see that the direction of pressure along the upper surface switches more frequently. Overall, for $L = 0.9$ and $L = 1.0$ shown in Fig. 20(a) and (b), the distribution of pressure difference could be divided into three parts, where both clamped ends and the midsection of the plate are subjected to upward and downward lift, respectively. In the pressure contour presented in Fig. 20(c), it is clear that the upper and lower surfaces of the front half of the flexible plate are simultaneously subjected to compressive forces, while the rear half is subjected to tensile forces. The pressure distribution curve indicates that the absolute values of the pressure coefficients on the upper and lower surfaces are approximately equal. Accordingly, the total lift experienced by the lower plate is nearly negligible, which better explains the very small lift $\overline{C}_L$ and strain energy E_s shown in Table III with $L/H = 120$. With L increased to 1.5, the upper surface of the plate experiences greater pressure gradient variations, resulting in more significant local pressure direction changes. The pressure contour plot in Fig. 20(d) shows a negative pressure region in the middle of the upper surface of the flexible plate, with positive pressure regions at both ends. This pressure distribution leads to a lower deformation amplitude in the middle of the plate compared to the sides.

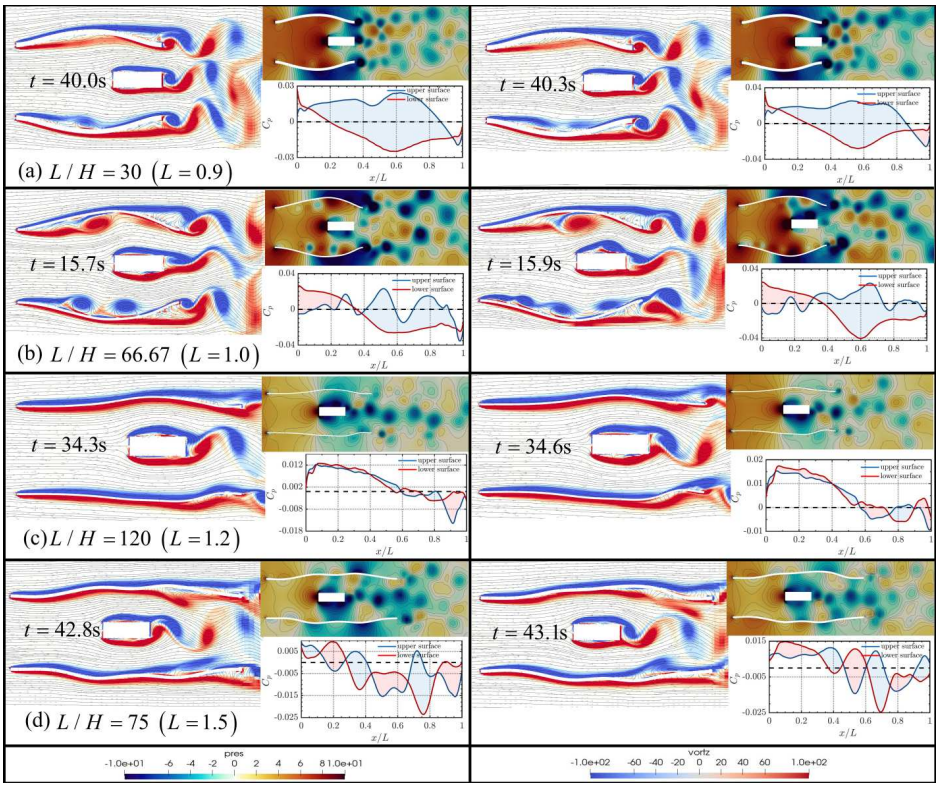

FIG. 20: Contours of vorticity at different aspect ratio L/H : (a) $L/H = 26.67$, (b) $L/H = 66.67$, (c) $L/H = 120$, (d) $L/H = 75$

4. Effect of Young's modulus of the plate on energy harvesting

In this section, to further investigate the material's behavior, particularly focusing on its influence on the structural response to fluid-induced vibrations, we study the effect of Young's modulus on energy harvesting performance. Young's Modulus E is varied from 8 to 20 MPa while fixing $L/H = 45$ and $Re = 400$. Fig. 21 depicts the variation of mean strain energy $\overline{E}_s$ with Young's modulus for the lower and upper plates. It should be noted that the strain energy variation trends of the upper and lower plates are approximately similar; specifically, the strain energy of the plates decreases with the increase of Young's modulus. Three typical cases are considered to further investigate the variations in the wake flow with different E. As seen from Fig. 21, when the value of

E is low, vortices continue to form on the leading edge of the plate and detach along the surface. Downstream of the plate and bluff body, the behavior of the vortices becomes more irregular and nonlinear, including vortex splitting and merging. As the value of E for the plate increases to 20 MPa, the vortex motion becomes more regular, with positive and negative vortices alternately detaching from the end of the plate and the rear edge of the bluff body.

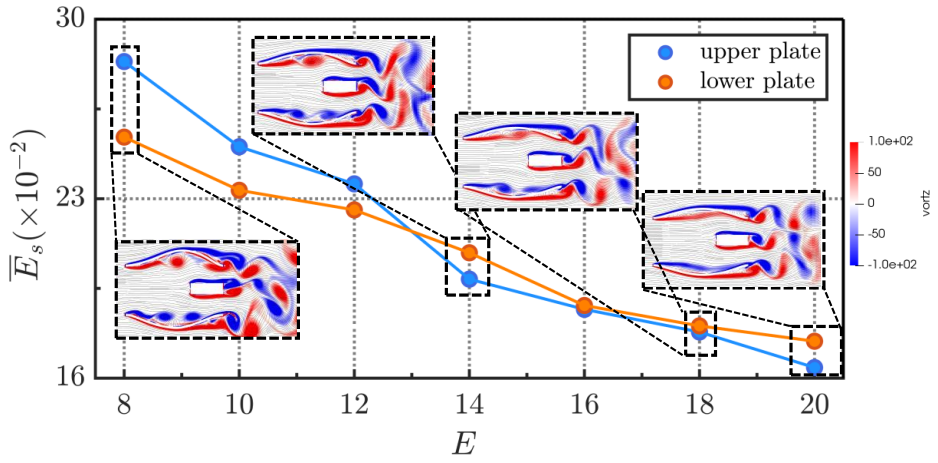

FIG. 21: Mean strain energy $\overline{E}_s$ and the wake pattern versus different Young's modulus E (MPa) of the two plates

To quantitatively explore the effects of E on the response of the flexible plate, the mean displacement y'_{m} at the position of maximum vibration amplitude and the total lift coefficient C_L of the lower plate are further analyzed, and the results are displayed in Fig. 22(a). As E increases from 8 MPa to 20 MPa, the mean displacement experienced by the lower plate generally decreases with the increase of Young's modulus. The variation trend of the average lift coefficient $\overline{C}_L$ is approximately opposite to that of y'_{m} with the change in E. As E increases, the values of $\overline{C}_L$ gradually rise, reaching a local maximum at $E = 14$Mpa. When E increases from 14 MPa to 16 MPa, the lift coefficient experiences a slight decrease, followed by a gradual increase. The dominant frequency of the flow field and the dynamic response of plates are further discussed due to the strong interaction between plate vibration and vortex shedding. Fig. 22(b) displays the variation trend of the dominant frequency f_L of the lift coefficient of the lower plate, the dominant frequency f_v of the vibration of the lower plate, and the dominant frequency f_s of the experience by the bluff body as E is increased. From Fig. 22(b), the vibration of the plate and the related flow field around

the flexible structure have approximately consistent dominant frequencies($f_v = f_L$), except for the case at $E = 20$Mpa. Furthermore, it should be noted that the flow field in the vicinity of the bluff body, the vibration of the plates, and the flow field around the plates all have the dominant frequency within the range of E from 8 to 14 MPa. This coherence in frequencies indicates a state of fluid-structure coupling, where the interactions between the fluid and the plate are synchronized. It is notable that, for $E = 12$ MPa and $E = 14$ MPa, there is a notable difference between the dominant frequencies of vortex shedding from the bluff body. As illustrated in Fig. 22(b), all cases can be divided into two regimes based on the values of f_s: between $E = 8$ and $E = 12$, the dominant frequencies of f_s are approximately 2.5 Hz, whereas between $E = 14$ and $E = 20$, the dominant frequencies of f_s are around 9 Hz. This indicates the interaction between the flow field and the vibration of the plates.

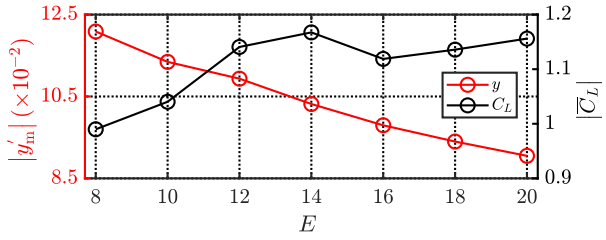

(a) The y'_m and $\overline{C}_L$ trends with the variation of different E.

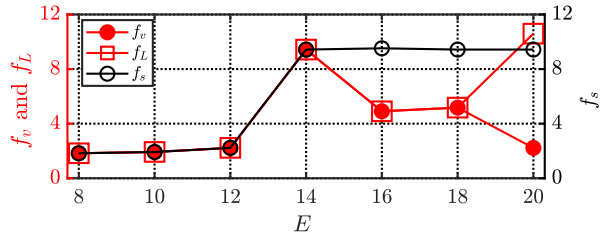

(b) The f_v, f_L and f_s trends with the variation of different E

FIG. 22: Characteristics of the flow field, plate structure at different Young's modulus E

To further clarify the mechanism of the plate vibration, the frequency spectra of the fluctuation of lift coefficient $C_L - \overline{C}_L$ of the lower plate, global displacement fluctuation $y - \overline{y}$, and the fluctuation of lift coefficient $C_f - \overline{C}_f$ of the bluff body are displayed in Fig. 23. From Fig. 23(a), all frequency spectra of the bluff body show two distinct peaks in the flow field response: a low-frequency signal around 2 Hz and a high-frequency signal around 10 Hz. This indicates the cou-

pling between the flexible structure and the bluff body in the flow field induces nonlinear effects and dynamic response variations in the flexible structure, thereby influencing the stability of the flow field. Based on the frequency spectrum patterns of the three fields at different Young's modulus E, they can be divided into three categories. In Fig. 23(b), in the flow field around the flexible structure with the range of E from 8 MPa to 14 MPa, aside from the dominant frequency, another frequency peak is observed in the flow response. This peak appears within the Fourier analysis bandwidth in the corresponding vibration spectrum of the flexible structure and the flow field spectrum around the bluff body. This demonstrates a total coupled state at these regimes. Furthermore, it can be noted from Fig. 23(b) that for $E = 16$ and $E = 18$, in addition to dominant frequency, there are two frequency peaks of $f = 9.709$Hz and $f = 10.351$Hz in the response of fields of the plates, respectively. These peaks exhibit multiple relationships with the dominant frequency. For $E = 20$Mpa, there are three distinct peaks of frequencies among three fields.

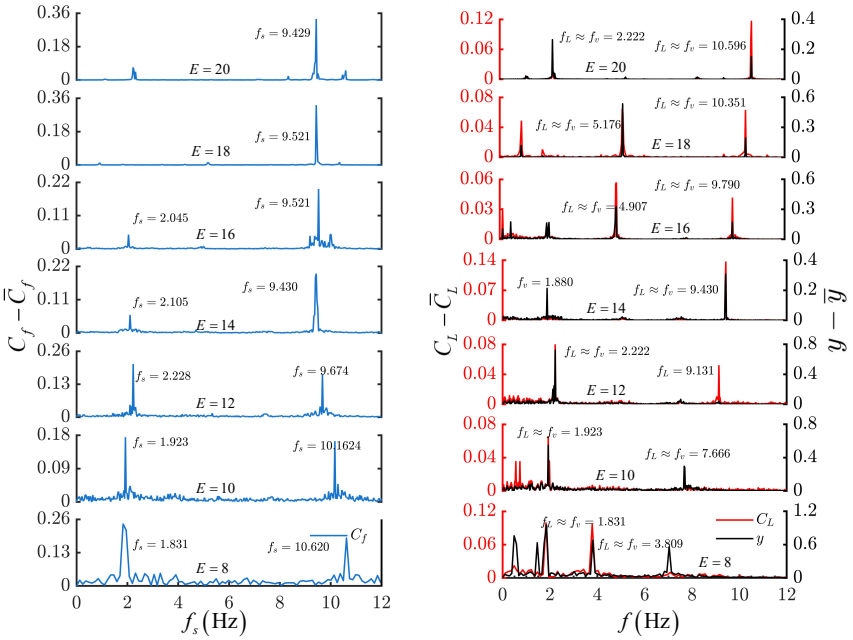

FIG. 23: Frequency characteristics of different structures: (a) the bluff body, (b) the plates

To sum up, when E is between 8 MPa and 14 MPa, the vortex shedding of the bluff body, the

vibration of the plate, and the flow field around the plate couple strongly with each other. For $E = 16$ MPa and $E = 18$ MPa, the flow field and the response of the plate are coupled with each other. Combining the wake pattern shown in Fig. 21, the vibration of the plate is mainly driven by the vortical structures moving along the surface of the plate and shedding from trailing edges in the regime of $E = 8$ MPa to $E = 18$ MPa. When $E = 20$ MPa, the three physical fields are not coupled, and the vibration response is dominated by structural natural frequency. Consequently, altering the Young's modulus of the flexible plate is significant for enhancing energy harvesting performance.

IV. CONCLUSION

In this work, we have presented preliminary results on improving the energy harvesting performance of clamped flexible plates using vortex shedding behind a fixed rigid bluff body. To the best of our knowledge, this is the first study of its kind in the literature. Specifically, we propose a novel configuration for the deformation of a flexible plate clamped at both ends in a flow field to harvest energy. This model utilizes vortex shedding behind the bluff body to induce plate deformation, thereby improving energy harvesting performance. Considering the strong interaction between the flow and the flexible structure with large deformation, a recently proposed stabilised immersed framework for fluid-flexible structure interaction has been adapted in this work. Based on numerous computational studies for a range of parameters of interest, the optimal location and geometry of the bluff body, the aspect ratio, and Young's modulus of the plate are identified at which the system can achieve higher energy harvesting performance. The effects of these design parameters are explored through computational studies by investigating the characteristics of plate structural response, the flow field, and the evolution of vortex shedding. This work can offer innovative potential by extending this application to new fields, particularly in understanding how wave loads affect structural deformation, stress distribution, and potential vibration modes. The main conclusions drawn from the results of the present work are summarised below.

Firstly, we found that the energy harvesting performance is affected by the variations of the location of the bluff body, which influences the response of the flow field and structure. As the bluff body moves downstream, the plate vibration and flow field experience more pronounced periodicity attributed to a pair of vortices alternately shedding from the bluff body within one cycle. Additionally, the vibration mode of the plate transitions from the second mode to the first

mode as the distance g of the bluff body from the leading edge of the plate increases. Therefore, we can achieve enhanced energy harvesting performance by moving the bluff body downstream from the leading edge of the flexible plates. *Secondly*, we focused on discussing the impact of the geometry of the bluff body on the performance of energy harvesting. At the location, $g = 0.6$, varying l/h reveals that the energy harvesting performance at $h = 0.1$ is better than that of other geometric configurations of the bluff body. As the h increases, the complexity of the interaction between the plate and the vortices shed behind the bluff body intensifies, leading to a more pronounced vorticity. The hydrodynamic performance is mainly influenced by h of the bluff body, in which the lift distribution along the x-axis displays comparable characteristics at the same h. When h is the same, the longer the length l of the bluff body, the more the complexity of the interaction between the plate and the vortices shed behind the bluff body intensifies, resulting in better energy harvesting performance. There are several vortex structures form and move along the surface of the plate when $h = 0.1$. *Thirdly*, we further investigated the influence of the aspect ratio (L/H) of the plate on energy harvesting performance. The critical value ($L/H = 45$) of the aspect ratio has been identified, at which the system obtains optimal energy harvesting performance, along with the maximum of the lift coefficient $\overline{C}_L$. The piezoelectric patches are recommended to be attached as closely as possible to the two clamped ends, where the local strain energy attains its maximum value. *Lastly*, Young's modulus of the plate greatly impacts its mechanical behaviour and strain energy. The dominant frequencies of the fluctuations of the lift coefficient of the bluff body at $E = 8 - 14$ MPa are consistent with the dominant frequencies of related fluctuations of the lift coefficient and the vibration of the plate. The vibration of the plate is mainly driven by the vortical structures moving along the surface of the plate and shedding from the leading and trailing edges in the regime of $E = 8$ MPa to $E = 18$ MPa, while the structural natural frequency dominates the vibration response at $E = 20$ MPa.

The preliminary results of the present work demonstrate an order of magnitude improvements in the strain energy of the clamped flexible plates by clever exploitation of vortex shedding behind a fixed bluff body. This study demonstrated the mechanism of energy harvesting from flow-induced vibrations of clamped flexible plates, offering a substantial foundation for further research on energy harvesters within fluid-flexible plate systems. We hope this work will spark new explorations into flexible plate systems and their energy-harvesting performance using clever mechanisms of vortex shedding. Further studies include a systematic characterization of energy harvesting performance for a wider range of non-dimensional parameters, including higher Reynolds

numbers and bluff bodies of various geometries, configurations and orientations.

REFERENCES

[1]C. W. Zheng, C. Y. Li, J. Pan, M. Y. Liu, and L. L. Xia, "An overview of global ocean wind energy resource evaluations," Renew. Sustain. Energy Rev. **53**, 1240–1251 (2016).

[2]N. Kannan and D. Vakeesan, "Solar energy for future world: - a review," Renew. Sustain. Energy Rev. **62**, 1092–1105 (2016).

[3]E. Segura, R. Morales, J. Somolinos, and A. López, "Techno-economic challenges of tidal energy conversion systems: Current status and trends," Renew. Sustain. Energy Rev. **77**, 536–550 (2017).

[4]N. Panwar, S. Kaushik, and S. Kothari, "Role of renewable energy sources in environmental protection: A review," Renew. Sustain. Energy Rev. **15**, 1513–1524 (2011).

[5]K. Kaygusuz, "Energy for sustainable development: A case of developing countries," Renew. Sustain. Energy Rev. **16**, 1116–1126 (2012).

[6]L. Zhang, A. Abdelkefi, H. Dai, R. Naseer, and L. Wang, "Design and experimental analysis of broadband energy harvesting from vortex-induced vibrations," J. Sound Vib. **408**, 210–219 (2017).

[7]W. Xu, M. Yang, E. Wang, and H. Sun, "Performance of single-cylinder vivace converter for hydrokinetic energy harvesting from flow-induced vibration near a free surface," Ocean Eng. **218**, 108168 (2020).

[8]A. Barrero-Gil, G. Alonso, and A. Sanz-Andres, "Energy harvesting from transverse galloping," J. Sound Vib. **329**, 2873–2883 (2010).

[9]L. Goyaniuk, D. Poirel, A. Benaissa, and H. Amari, "The energy extraction potential from pitch-heave coupled flutter," J. Sound Vib. **555**, 117714 (2023).

[10]P. Han, Q. Huang, G. Pan, D. Qin, W. Wang, R. T. Gonçalves, and J. Zhao, "Optimal energy harvesting efficiency from vortex-induced vibration of a circular cylinder," Ocean Eng. **282**, 114869 (2023).

[11]A. Mehmood, A. Abdelkefi, M. Hajj, A. Nayfeh, I. Akhtar, and A. Nuhait, "Piezoelectric energy harvesting from vortex-induced vibrations of circular cylinder," J. Sound Vib. **332**, 4656–4667 (2013).

[12]Z. Rong, B. Cao, and J. Hu, "Stability analysis on an aeroelastic system for design of a flutter

energy harvester," Aerosp. Sci. Technol. **60**, 203–209 (2017).

[13]Y. Ma, Y. Luan, and W. Xu, "Hydrodynamic features of three equally spaced, long flexible cylinders undergoing flow-induced vibration," Eur. J. Mech. B/Fluids. **79**, 386–400 (2020).

[14]C. Bao, Y. Dai, P. Wang, and G. Tang, "A piezoelectric energy harvesting scheme based on stall flutter of airfoil section," Eur. J. Mech. B/Fluids. **75**, 119–132 (2019).

[15]A. Abdelkefi, M. Ghommem, A. Nuhait, and M. Hajj, "Nonlinear analysis and enhancement of wing-based piezoaeroelastic energy harvesters," J. Sound Vib. **333**, 166–177 (2014).

[16]L. Tang, M. P. Païdoussis, and J. Jiang, "Cantilevered flexible plates in axial flow: Energy transfer and the concept of flutter-mill," J. Sound Vib. **326**, 263–276 (2009).

[17]D. Cao, J. Wang, X. Guo, S. Lai, and Y. Shen, "Recent advancement of flow-induced piezoelectric vibration energy harvesting techniques: principles, structures, and nonlinear designs," Appl. Math. Mech. **43**, 959–978 (2022).

[18]J. Wang, C. Zhang, S. Gu, K. Yang, H. Li, Y. Lai, and D. Yurchenko, "Enhancement of low-speed piezoelectric wind energy harvesting by bluff body shapes: Spindle-like and butterfly-like cross-sections," Aerosp. Sci. Technol. **103**, 105898 (2020).

[19]M. Eugeni, H. Elahi, F. Fune, L. Lampani, F. Mastroddi, G. P. Romano, and P. Gaudenzi, "Numerical and experimental investigation of piezoelectric energy harvester based on flag-flutter," Aerospace Sci. Technol. **97**, 105634 (2020).

[20]J. Wang, L. Geng, K. Yang, L. Zhao, F. Wang, and D. Yurchenko, "Dynamics of the double-beam piezo–magneto–elastic nonlinear wind energy harvester exhibiting galloping-based vibration," Nonlinear Dyn. **100**, 1963–1983 (2020).

[21]K. Yang, J. Wang, and D. Yurchenko, "A double-beam piezo-magneto-elastic wind energy harvester for improving the galloping-based energy harvesting," Appl. Phys. Lett. **115**, 193901 (2019).

[22]M. Hafizh, A. G. Muthalif, J. Renno, M. Paurobally, and M. S. Mohamed Ali, "A vortex-induced vibration-based self-tunable airfoil-shaped piezoelectric energy harvester for remote sensing applications in water," Ocean Eng. **269**, 113467 (2023).

[23]W. Liao, Y. Wen, J. Kan, X. Huang, S. Wang, Z. Li, and Z. Zhang, "A joint-nested structure piezoelectric energy harvester for high-performance wind-induced vibration energy harvesting," Int. J. Mech. Sci. **227**, 107443 (2022).

[24]G. Hu, K. Tse, M. Wei, R. Naseer, A. Abdelkefi, and K. Kwok, "Experimental investigation on the efficiency of circular cylinder-based wind energy harvester with different rod-shaped

attachments," Appl. Energy. **226**, 682–689 (2018).

[25]L. Zhao and Y. Yang, "An impact-based broadband aeroelastic energy harvester for concurrent wind and base vibration energy harvesting," Appl. Energy. **212**, 233–243 (2018).

[26]S. Ravi and A. Zilian, "Simultaneous finite element analysis of circuit-integrated piezoelectric energy harvesting from fluid-structure interaction," Mech. Syst. Signal Process. **114**, 259–274 (2019).

[27]U. Latif, E. H. Dowell, E. Uddin, and M. Yamin Younis, "Parametric aerodynamic and aeroelastic study of a deformable flag-based energy harvester for powering low energy devices," Energy Convers. Manag. **280**, 116846 (2023).

[28]B. S. H. Connell and D. K. P. Yue, "Flapping dynamics of a flag in a uniform stream," J. Fluid Mech. **581**, 33–67 (2007).

[29]C. Eloy, R. Lagrange, C. Souilliez, and L. Schouveiler, "Aeroelastic instability of cantilevered flexible plates in uniform flow," J. Fluid Mech. **611**, 97–106 (2008).

[30]J. Ryu, S. G. Park, B. Kim, and H. J. Sung, "Flapping dynamics of an inverted flag in a uniform flow," J. Fluids Struct. **57**, 159–169 (2015).

[31]J. Allen and A. Smits, "Energy harvesting eel," J. Fluids Struct. **15**, 629–640 (2001).

[32]U. Latif, E. Uddin, M. Younis, J. Aslam, Z. Ali, M. Sajid, and A. Abdelkefi, "Experimental electro-hydrodynamic investigation of flag-based energy harvesting in the wake of inverted c-shape cylinder," Energy **215**, 119195 (2021).

[33]K. Singh, S. Michelin, and E. De Langre, "The effect of non-uniform damping on flutter in axial flow and energy-harvesting strategies," Proc. R. Soc. A: Math. Phys. Eng. Sci. **468**, 3620–3635 (2012).

[34]U. Latif, M. Y. Younis, S. Idrees, E. Uddin, A. Abdelkefi, A. Munir, and M. Zhao, "Synergistic analysis of wake effect of two cylinders on energy harvesting characteristics of piezoelectric flag," Renew. Sustain. Energy Rev. **173**, 113114 (2023).

[35]K. Shoele and R. Mittal, "Energy harvesting by flow-induced flutter in a simple model of an inverted piezoelectric flag," J. Fluid Mech. **790**, 582–606 (2016).

[36]M. Piñeirua, O. Doaré, and S. Michelin, "Influence and optimization of the electrodes position in a piezoelectric energy harvesting flag," J. Sound Vib. **346**, 200–215 (2015).

[37]Z. Zhou, W. Qin, P. Zhu, W. Du, W. Deng, and J. Pan, "Scavenging wind energy by a dynamic-stable flutter energy harvester with rectangular wing," Appl. Phys. Lett. **114**, 243902 (2019).

[38]D. Kim, J. Cossé, C. Huertas Cerdeira, and M. Gharib, "Flapping dynamics of an inverted flag,"

J. Fluid Mech. **736**, R1 (2013).

[39]I. Collins, M. Hossain, W. Dettmer, and I. Masters, "Flexible membrane structures for wave energy harvesting: A review of the developments, materials and computational modelling approaches," Renew. Sustain. Energy Rev. **151**, 111478 (2021).

[40]C. Kadapa, W. Dettmer, and D. Perić, "A stabilised immersed framework on hierarchical b-spline grids for fluid-flexible structure interaction with solid–solid contact," Comput. Methods Appl. Mech. Eng. **335**, 472–489 (2018).

[41]C. Kadapa, W. Dettmer, and D. Perić, "A stabilised immersed boundary method on hierarchical b-spline grids for fluid–rigid body interaction with solid–solid contact," Comput. Methods Appl. Mech. Eng. **318**, 242–269 (2017).

[42]C. Kadapa, W. G. Dettmer, and D. Perić, "Accurate iteration-free mixed-stabilised formulation for laminar incompressible navier–stokes: Applications to fluid–structure interaction," J. Fluids Struct. **97**, 103077 (2020).

[43]C. Kadapa, W. Dettmer, and D. Perić, "On the advantages of using the first-order generalised-alpha scheme for structural dynamic problems," Comput. Struct. **193**, 226–238 (2017).

[44]W. G. Dettmer and D. Perić, "A new staggered scheme for fluid–structure interaction," Int. J. Numer. Methods Eng. **93**, 1–22 (2013).

[45]C. Kadapa, "A second-order accurate non-intrusive staggered scheme for the interaction of ultra-lightweight rigid bodies with fluid flow," Ocean Eng. **217**, 107940 (2020).

[46]C. Kadapa, X. Wang, and Y. Mei, "A comprehensive assessment of accuracy of adaptive integration of cut cells for laminar fluid-structure interaction problems," Comput. Math. Appl. **122**, 1–18 (2022).

[47]S. Turek and J. Hron, "Proposal for numerical benchmarking of fluid-structure interaction between an elastic object and laminar incompressible flow," in *Fluid-Structure Interaction*, edited by H.-J. Bungartz and M. Schäfer (Springer Berlin Heidelberg, Berlin, Heidelberg, 2006) pp. 371–385.